Published in final edited form as:
*Biomacromolecules*. 2013 May 13; 14(5): 1349–1360. doi:10.1021/bm302000n.

# Engineering the Microstructure of Electrospun Fibrous Scaffolds by Microtopography

**Qian Cheng**[1,#], **Benjamin L.-P. Lee**[2,#], **Kyriakos Komvopoulos**[1,*], and **Song Li**[2]

[1]Department of Mechanical Engineering, University of California, Berkeley, California 94720, United States

[2]Department of Bioengineering, University of California, Berkeley, California 94720, United States

## Abstract

Controlling the structure and organization of electrospun fibers is desirable for fabricating scaffolds and materials with defined microstructures. However, the effects of microtopography on the deposition and, in turn, the organization of the electrospun fibers are not well understood. In this study, conductive polydimethylsiloxane (PDMS) templates with different micropatterns were fabricated by combining photolithography, silicon wet etching, and PDMS molding techniques. The fiber organization was varied by fine-tuning the microtopography of the electrospinning collector. Fiber conformity and alignment were influenced by the depth and the slope of microtopography features, resulting in scaffolds comprising either an array of microdomains with different porosity and fiber alignment or an array of microwells. Microtopography affected the fiber organization for hundreds of micrometers below the scaffold surface, resulting in scaffolds with distinct surface properties on each side. In addition, the fiber diameter was also affected by the fiber conformity. The effects of the fiber arrangement in the scaffolds on the morphology, migration, and infiltration of cells were examined by *in vitro* and *in vivo* experiments. Cell morphology and organization were guided by the fibers in the microdomains, and cell migration was enhanced by the aligned fibers and the three-dimensional scaffold structure. Cell infiltration was correlated with the microdomain porosity. Microscale control of the fiber organization and the porosity at the surface and through the thickness of the fibrous scaffolds, as demonstrated by the results of this study, provides a powerful means of engineering the three-dimensional structure of electrospun fibrous scaffolds for cell and tissue engineering.

## 1. INTRODUCTION

Electrospinning of polymer fibers is a simple and cost-effective method of fabricating fibrous structures.[1,2] Electrospinning of polymer fibrous scaffolds that resemble the structure and function of extracellular matrix has been explored for various biomedical applications,[3-10] such as wound healing,[7] drug delivery,[7] and tissue engineering.[8-10] Fibrous scaffolds with well-controlled patterned structures are of particular significance in cell biology and scaffold engineering. For example, scaffolds with aligned fibers may influence cell function, such as migration, organization, and differentiation.[11-15] Scaffolds with microwell arrays are of importance in the fabrication of uniform cell arrays.[16] Fibrous structures exhibiting sufficient porosity are desirable in scaffold engineering because porosity plays an important role in cell infiltration and tissue remodeling.[17-21]

[*]Corresponding Author: Tel: 1-510-642-2563; Fax: 1-510-642-5539; kyriakos@me.berkeley.edu.
[#]These authors have contributed equally to this work.

**Supporting Information Available**
This material is available free of charge via the Internet at http://pubs.acs.org.

Various methods have been developed to control fiber alignment and other types of structure.[1,2,22] A common approach to increase the porosity of electrospun fibrous scaffolds is to incorporate sacrificial structures, such as salt grains or other porogens, which can be easily removed at a later stage; however, leaching of the sacrificial structure is often accompanied by pore collapse.[17] Other approaches for addressing the porosity issue include multilayering of fibers,[18] tailoring of the fiber diameter,[19] incorporation of sacrificial fibers,[20] and post-processing by laser ablation.[21] Traditionally, structures with microwell arrays have been produced by polymer molding.[16] Despite several attempts to fabricate microwells by electrospinning on templates consisting of metal spheres, controlling the size and shape of microwells has been problematic.

Polymer fiber electrospinning onto special templates has been proven to be an effective method of fabricating fibrous constructs with defined fiber organization.[5,22-28] Templates with two-dimensional (2D) and three-dimensional (3D) micropatterns produced from surface-machined metal and ice substrates[24-28] or metal wire networks[5,26] have been used to control the fiber density and alignment in constructs. However, these methods are slow, costly, difficult to control, and do not yield a wide range of scalable pattern geometries, as summarized in Table 1. Polydimethylsiloxane (PDMS) templates with surface micropatterns produced by photolithography have been used to overcome these drawbacks,[29] but with limited success in controlling the fiber density and orientation. In addition, control of the fiber conformity (i.e., the ability of the fibers to closely follow and replicate the surface of the PDMS collector) on micropatterned surfaces is not well understood. Therefore, the objectives of this study were to develop a versatile method of fabricating conductive PDMS templates with 3D micropatterns, investigate if the micropattern geometry (microtopography) and electrospinning condition (i.e., feed rate of the polymer solution) can be used to regulate the fiber conformity and alignment to produce scaffolds with distinct structures, and examine the effects of the fabricated scaffolds on the morphology, migration, and infiltration of the cells.

## 2. MATERIALS AND METHODS

### 2.1. Fabrication of Conductive Micropatterned PDMS Templates

The fabrication process of the conductive PDMS templates used in this study is shown in Figure 1. The back side of a ~525-μm-thick p-type Si(100) wafer with both of its sides coated with a ~0.6-μm-thick SiN layer, was spin coated with a 4-μm-thick layer of OCG 825 photoresist (PR) (Figure 1a). After the exposure to UV light through the windows of a Cr mask (Figure 1b) (Karl Suss MA6 Mask Aligner, Karl Suss America, Waterbury, VT) and development, the micropattern was transferred to the PR (Figure 1c) and then to the SiN layer at the back side of the wafer by reactive ion etching (Figure 1d) (Technics PE II-A, Plasma Equipment Technical Services, Livermore, CA). Following stripping of the PR (Figure 1e), the exposed Si was etched to a depth of ~500 μm in 30% KOH at 85°C (Figure 1f1 and f2), and the SiN layer was etched away by immersing the wafer into a bath of 49% HF for 2 h (Figure 1g). Subsequently, the master wafer was exposed to perfluoro-1,1,2,2-tetrahydrooctyl-trichlorosilane (United Chemical Technology, Bristol, PA) vapor in a desiccator overnight to prevent the adhesion of the PDMS template. A mixture (10:1) of Sylgard 184 silicone elastomer components (Dow Corning, Midland, MI) was then transferred onto the master wafer (Figure 1h) and cured at 65°C overnight to fabricate a micropatterned PDMS template (Figure 1i). To increase the conductivity of the PDMS template, carbon black (Vulcan XC-72R, Fuel Cell Store, Boulder, CO) was introduced into the silicone mixture (12.5% w/v). Because of the highly viscous mixture, the master wafer was placed in vacuum for 1 h to allow the mixture to completely fill up the features on the wafer surface before curing. After curing overnight at 65°C, the PDMS template was peeled off from the master wafer and used to fabricate the fibrous scaffolds.

### 2.2 Fabrication of Fibrous Scaffolds

Fibrous scaffolds were fabricated from biodegradable poly(L-lactide) (PLLA) (Lactel Absorbable Polymers, Pelham, AL) of inherent viscosity equal to 1.09 dL/g (Lactel Absorbable Polymers, Pelham, AL). PLLA pellets were first dissolved in hexafluoroisopropanol (19% w/v) in an ultrasonic water bath. The polymer solution was then delivered through a stainless steel 23G dispensing needle by a syringe pump.[11-13] By applying a voltage of 12 kV to the needle with a high-voltage generator, electrostatically charged PLLA fibers of tens of nanometers up to ~2 μm in average diameter were ejected from the charged needle toward the surface of a grounded template (fixed at 8 cm from the needle tip) at a feed rate in the range of 0.2–2 mL/h. Then, the construct produced by the polymer fibers deposited onto the template was lifted off from the PDMS template. A flat PDMS template without any surface features was used to fabricate control samples under the same electrospinning condition. For cell studies, fibrous scaffolds were fabricated at a fixed feed rate of 1.0 mL/h.

The pattern geometry of the PDMS templates, the diameter, distribution, and arrangement of the fibers on the micropatterned PLLA scaffolds, and cross-sectional samples of the fabricated scaffolds were examined with a field emission scanning electron microscope (SEM) (TM-1000, Hitachi, Pleasanton, CA) operated at an acceleration voltage of 15 kV without coating the samples with a metal layer. The overall fiber density distribution was examined with an upright microscope (Zeiss HAL 100, Carl Zeiss MicroImaging, Thornwood, NY). Cross-sectional samples for SEM imaging were prepared by cutting the PLLA scaffolds with a laser.[21] Before *in vitro* cell or tissue seeding and implantation into the subcutaneous cavity of rats, the scaffolds were sterilized in 70% ethanol under the effect of ultraviolet light for 30 min and then washed 5 times with sterile phosphate buffered saline (PBS).

### 2.3. Cell Culture and Morphology Analysis

Human mesenchymal stem cells (hMSCs) (Lonza Walkersville, Walkersville, MD) were cultured in hMSC maintenance medium (MSCGM, Cambrex, East Rutherford, NJ) and maintained in a humidified incubator with 5% $CO_2$ at 37°C. Before cell seeding, scaffolds sterilized as described above were washed with sterile deionized water, coated with 1% fibronectin (Sigma-Aldrich, St. Louis, MO) for 30 min at 37°C, and washed with PBS. hMSCs of a number density equal to ~3,000 cells/$cm^2$ were seeded with hMSC maintenance medium and cultured for 24 h. Then, the cells were fixed with 4% paraformaldehyde (PFA) and permeabilized with 0.5% Triton X-100. To observe the cell morphology, the actin structure and nuclei of hMSCs were stained with Alexa-Phalloidin 488 and 4',6-diamidino-2-phenylindole (DAPI), respectively. Fluorescence images of the stained hMSCs were obtained with a confocal microscope (Zeiss LSM710, Carl Zeiss MicroImaging, Thornwood, NY) at 20× magnification and *z*-distance between cross-sections of 3–5 μm. Fluorescence signals from the entire stack were then projected onto a single plane to construct an overall image.

A 2D fast Fourier transform (FFT) was used to analyze the directionality of actin alignment, as described elsewhere.[14] Briefly, fluorescent images of the seeded hMSCs on the micropatterned scaffolds were converted to gray scale and masked with a circular pattern using Adobe Photoshop (Adobe, San Jose, CA). The images were subsequently imported into Image J software for 2D FFT analysis. Images were processed, transformed (rotated 90° clockwise), and analyzed using the oval-profile Image J plugin (courtesy of Bill O'Connell, http://rsbweb.nih.gov/ij/plugins/oval-profile.html). For consistency, the pixel intensity data in each intensity-distribution histogram were normalized by the lowest value and 1 was

subtracted from each data such that the lowest value was reassigned as 0. Graphical representations of actin alignment were obtained for pixel intensities between 0° and 180°.

### 2.4. Cell Proliferation Assay

To examine the hMSC proliferation rate, scaffolds prepared as described above were seeded with hMSCs of a number density equal to ~10,000 cells/cm$^2$ in Dulbecco's modified Eagle medium (DMEM) (Invitrogen, Carlsbad, CA) supplemented with 10% fetal bovine serum (Thermo Fisher Scientific, Waltham, MA) and 1% penicillin/streptomycin antibiotic mixture. After seeding for 24 h, the cells were fixed with 4% PFA, permeabilized with 0.5% Triton X-100, blocked with 3 mg/mL bovine serum albumin (BSA) and 0.1% Triton X-100, and stained with the proliferation marker Ki67 (Abcam, Cambridge, MA) in conjunction with DAPI nuclear counterstain. Fluorescent signals were obtained with the Zeiss LSM710 confocal microscope. Positive stained hMSCs were quantified with the Scion Image software (Scion, Fredrick, MD). The percentage of hMSCs that were in the active phase of the cell cycle was correlated to the proliferation rate.

### 2.5. Cell Migration Assay

For the cell migration studies, dorsal root ganglion (DRG) tissues were harvested from P4 rats and briefly maintained in neurobasal (NB) medium supplemented with B27 and 0.5 mM of L-glutamine (Invitrogen, Carlsbad, CA) prior to seeding onto the micropatterned scaffolds. Scaffolds were first sterilized and then coated with laminin (5 μg/cm$^2$) (Invitrogen, Carlsbad, CA) for 1 h at 37°C and washed with PBS before seeding. After seeding with a minimal volume of supplemented NB medium, the DRG tissues were incubated for 2 h and allowed to settle and attach to the scaffold surfaces. Sufficient medium was added afterwards to culture the DRG tissues on the fibrous scaffolds for 10 days, with the medium partially changed every 3 days. The samples were fixed after a 10-day culture with 4% PFA, permeabilized with 0.5% Triton X-100, blocked with BSA and 0.1% Triton X-100, and, subsequently, stained with anti-S-100 (β-subunit) (Sigma-Aldrich, St. Louis, MO) antibody for Schwann cells and counterstained with DAPI for cell nuclei. Fluorescence signals were obtained with the Zeiss LSM710 confocal microscope at 10× magnification and *z*-distance between cross-sections of 4-6 μm. Fluorescence signals from the entire stack were then projected onto a single plane to construct an overall image.

### 2.6. Cell Infiltration *In Vivo*

All experimental procedures with animals were approved by the Animal Care and Use Committee of the University of California, Berkeley. Micropatterned PLLA scaffolds were cut into 0.5 × 0.5 cm$^2$ samples, and 3 samples of each group were implanted into the subcutaneous cavity of Sprague-Dawley rats (Charles River Laboratories, Wilmington, MA) for 7 days using the following procedure. First, the rats were anesthetized with isofluorane and the incision sites were marked and disinfected with 70% ethanol. Then, incisions were made on the wall of the lower abdominal region, and PLLA scaffolds with different micropatterns were implanted into the incision sites and tucked subcutaneously away from the incision, with the back side of the scaffolds facing the muscle side. Cuts were sewed with interrupted 5-0 Monocryl (Ethicon, Somerville, NJ) mattress sutures. All rats were monitored daily, with no adverse incidents observed with any of them. The rats were returned to the operating room on the seventh day, where they were given general anesthesia and an overdose of euthanasia solution. Then, the implants with the attached surrounding tissue were removed, fixed with 4% PFA, and embedded in an optimal-cutting-temperature compound (TissueTek, Elkhart, IN), which was placed on dry ice. Transverse cross-sectional samples of 12 μm in thickness were obtained with a cryosectioner at −20°C, fixed with 4% PFA, stained with DAPI, and examined under a microscope (TE 300, Nikon, Melville, NY).

## 3. RESULTS AND DISCUSSION

While Si wet etching usually only produces specific slopes and shapes, distinct geometries with different depths, slopes, and aspect ratios were obtained in this study by controlling the etching process. Carbon black was added to fabricate conductive PDMS membranes with different patterned geometries that served as templates for electrospinning. The resulting electrospun PLLA scaffolds consist of an array of microdomains with varying features, such as fiber alignment and density, which are important factors for locally regulating cell organization and infiltration. The microstructure gradients produced within the scaffold thickness by the present fabrication process yield different surface microtopographies and properties (e.g., porosity) on each scaffold side, which could be advantageous for various tissue engineering applications.

### 3.1. Fabrication of Conductive Micropatterned PDMS Templates

Different structures were produced on the master wafer by KOH wet etching, depending on the width of the SiN layer between adjacent surface features (Figure 1f1 and f2), which were then transferred to the PDMS template. For a relatively wide SiN layer between nearby features, KOH anisotropic etching of Si(100) yielded micropatterns of rectangular pyramids with a sidewall slope of 54.7° with respect to the surface plane (Figure 1f1). However, in the case of a relatively narrow SiN layer, undercutting during KOH etching in the Si(111) direction and high etching rates in both Si(100) and Si(110) directions yielded rectangular pyramids with double-slope sidewalls (Figure 1f2). Thus, by varying the width of the SiN layer between micropattern features along each in-plane direction, different micropattern geometries were etched on the Si(100) wafer and then transferred to the molded PDMS templates. An etching mode (Figure 1f1) produced PDMS templates with taller pyramids (posts) possessing steep single-slope sidewalls, whereas another etching mode (Figure 1f2) yielded PDMS templates with shorter pyramids of less steep double-slope sidewalls.

### 3.2. Characterization of Micropatterned Templates

In-plane cross-sectional schematics of PDMS templates with micropatterns of different dimensions are shown Figure 2a–c, while corresponding SEM micrographs are shown in Figure 2d–i. Molds with cross-sections with both in-plane directions similar to those shown in Figure 1f1 and f2 produced micropatterned templates consisting of rectangular pyramids with steep single-slope sidewalls (pattern I, Figure 2a, d, and g) and shallow double-slope sidewalls (pattern II, Figure 2b, e, and h), respectively. However, molds with cross-sections similar to that shown in Figure 1f1 in one direction and similar to that shown in Figure 1f2 in the other direction produced micropatterned templates with prismatic pyramids having steep single-slope and shallow double-slope sidewalls in corresponding directions (pattern III, Figure 2c, f, and i).

### 3.3. Fiber Organization on Different Micropatterned Templates

Figure 3 shows PLLA scaffolds fabricated from PDMS templates with patterns I, II, and III. Figure 3a1, b1, and c1 are schematics of PLLA fibers forced by electrostatic forces to conform onto the micropattern features of the PDMS templates, whereas Figure 3a2–c3 and a4–c6 show SEM micrographs of the back side (facing the PDMS templates) and front side of the fabricated scaffolds, respectively.

As mentioned earlier, fiber conformity is defined as the ability of the fibers to replicate the surface of the PDMS collector. Tall pyramids with steep single-slope sidewalls (pattern I, Figure 2d and g) produced scaffolds conformal to the template micropattern only at the top of the tall pyramidal posts, resulting in the bridging of neighboring posts by aligned fibers (Figure 3a1). These scaffolds comprised small and shallow microwells with dense fibrous

structures, surrounded by arrays of less dense, aligned fibers in the diagonal, horizontal, or vertical direction (Figure 3a2 and a3). This micropattern of fibers gradually disappeared with the increase of the scaffold thickness with the electrospinning time (Figure 3a4–a6). In contrast, pattern II with short pyramidal posts exhibiting shallow double-slope sidewalls (Figure 2e and h) produced scaffolds conformal to the sidewalls except at the bottom of the microwells (Figure 3b1). These scaffolds consisted of uniformly distributed pyramidal microwells of densely packed fibers, surrounded by narrow rectangular arrays of relatively less dense fibers aligned perpendicular to the array sides (Figure 3b2 and b3). Scaffolds made with pattern III that had different micropattern geometries along the in-plane directions (Figure 2f and i) exhibited features that were combinations of those produced on the scaffolds fabricated from the templates shown in Figure 2a and b. The fibers of these scaffolds were densely packed along the short post/small sidewall slope direction and aligned along the tall post/high sidewall slope direction (Figure 3c2 and c3).

Figure 3a4–c6 show the front sides of PLLA scaffolds fabricated with different templates for different deposition times. Increasing the deposition time from 1 to 4 min had a diminishing effect on the micropattern transfer to the front side of the scaffolds, resulting in more randomly oriented fibers than those at the back side, especially for thicker scaffolds, i.e., 4 min deposition time (Figure 3a6, b6, and c6). Thus, scaffolds fabricated with the present method exhibited a gradient in the through-thickness microstructure.

### 3.4. Effect of Electrostatic Force on Fiber Conformity

Fiber electrospinning on an electrically conductive template containing post structures results in preferential fiber deposition over the posts due to the higher electrostatic forces applied to the fibers at the top of the posts than in any other region of the template surface.[26] Both fiber deposition and alignment were found to depend on the overall post geometry (i.e., post height and sidewall slope) and, presumably, the distance between posts. However, because all of the templates had a similar feature distance, fiber deposition and alignment demonstrated a dependence only on the post height and sidewall slope (Figure 2a–c). In particular, fiber deposition at the top of the posts and fiber alignment in the areas between posts was only observed for relatively tall posts with a large sidewall slope of pattern I (Figure 3a1), whereas for short posts with shallow double-slope sidewalls of pattern II, fiber deposition occurred in dense configurations over the entire post surface, closely following the surface micropattern of the template (Figure 3b1).

Fiber deposition and conformity strongly depend on the magnitude of the electrostatic force between the fibers and the template. The scaffolds shown in Figure 3 indicate that low posts with small sidewall slopes resulted in high electrostatic forces that enhanced the fiber conformity with the micropatterned template surface. This was confirmed by simulation results of the electrostatic potential field obtained with conductive PDMS templates possessing different micropattern geometries (see Supporting Information). Under these conditions, conformal fiber deformation resulted in full coverage of the entire post structure by densely packed fibers, except at the bottom of the microwells where the fibrous structure was less dense. Alternatively, for templates having tall posts with steep sidewalls (i.e., pattern I), the pattern geometry could not be fully accommodated by fiber deformation between posts due to significant changes in the feature dimensions and the weaker electrostatic force at these regions. This resulted in fiber bridging and, consequently, fiber alignment in the areas between posts. For the template features examined in this study, the critical post height for full post coverage by the fibers was found to be between 325 and 375 μm. Moreover, because the overall electrostatic force applied to the fibers decreased with the increase of the scaffold thickness due to the repulsive force exerted by the deposited fibers having the same type of charge, more random and dense fibers were obtained with

thicker scaffolds, as evidenced by the progressive decrease of the contrast of the fiber structures shown in Figure 3a4–c6.

### 3.5. Effect of Fiber Organization on Fiber Density

Optical microscopy photographs of the back (Figure 4a–c) and front (Figure 4d–f) sides of PLLA fibrous scaffolds fabricated from PDMS templates with different micropatterns provided important information about the density of the produced fibrous structures. Differences in brightness may be associated with local variations in the fiber density. Tall posts with steep single-slope sidewalls (pattern I) produced dense fibrous structures only over the posts, and less dense structures consisting of aligned fibers between the posts (Figure 4a and d). However, low posts with shallow double-slope sidewalls (pattern II) were fully covered by dense fibrous structures (Figure 4b and e), while posts with different post heights and sidewall slopes in the in-plane directions (pattern III) produced hybrid scaffolds (Figure 4c and f). These findings indicate that fiber organization in various microdomains resulted in different fiber densities and, in turn, scaffold porosities.

### 3.6. Through-thickness Variation of the Scaffold Structure

Scaffold cross-sections shown in Figure 5 provide further insight into the effect of surface micropatterning on the through-thickness scaffold structure. While the structure of the flat (control) scaffold does not show significant through-thickness variation (Figure 5a), the micropatterned scaffolds show significant spatial variation in fiber density. Specifically, posts with steep sidewalls (pattern I and III) demonstrate densely deposited fibers over the posts and fiber bridging between posts (Figure 5b and d, respectively), while posts with small sidewall slopes (pattern II) show dense fiber deposition over whole posts except at the bottom of the scaffold (Figure 5c). In addition, the increase of the scaffold thickness produced gradual changes in the fiber organization through the scaffold thickness (Figure 5b–d). For patterns I and III, the scaffolds comprise heterogeneous porous structures of loosely aligned fibers at the back side and densely packed and randomly oriented fibers at the front side (Figure 5b and d). A comparison of the fibrous structures shown in Figure 5 indicates that the micropatterned PLLA scaffolds exhibit higher porosity (Figure 5c) or both higher porosity and fiber alignment (Figure 5b and d) compared to the flat PLLA scaffolds (Figure 5a).

### 3.7. Effect of Fiber Diameter and Deformability on Fiber Conformity

To examine the dependence of the scaffold structure on the fiber deformability (for a given template), fiber electrospinning on the template with tall posts and steep single-slope sidewalls (pattern I) was carried out at different solution feed rates and a voltage of 12 kV. High-resolution SEM images of fibers electrospun onto a flat region of this template at a feed rate of 0.2, 0.5, and 2.0 mL/h are shown in Figure 6a, b, and c, respectively. The observed gradual increase of the average fiber diameter with the increase of the feed rate, shown in Table 2, is consistent with a previous study.[28] Figure 6d–f shows that the increase of the fiber diameter resulted in less post area coverage by the fibers and the formation of shallower microwells. The depth of the microwells shown in Figure 6g, h, and i is approximately equal to 270, 230, and 190 μm, respectively. This trend can be attributed to the increase of the solution volume charge with the decrease of the feed rate,[30] resulting in thinner fibers, which easily deformed to conform to the micropattern features and the higher attractive force between the charged fibers and the grounded template. Therefore, the decrease of the fiber diameter with the feed rate enhanced the fiber conformity to the micropatterned template surface, resulting in a larger area of post coverage by a dense fiber structure and the formation of deeper microwells (Figure 6g–i).

### 3.8. Effect of Micropatterned Scaffolds on Cell Morphology, Organization, and Proliferation

Figure 7 shows the effect of scaffold micropatterning on the actin morphology, alignment, and proliferation rate of hMSCs. The control sample (Figure 7a) and the sample with pattern II characterized by microwell arrays with randomly oriented fibers (Figure 7c) do not show actin alignment with the fibers. In contrast, actin alignment along the fiber direction can be observed on the scaffolds demonstrating fiber alignment at specific surface regions (Figure 7b and d). Patterns I and III with specific fiber alignment at distinct regions (Figure 7b and d) produced FFT pixel intensity distribution curves with peaks corresponding to the observed actin alignment along the fiber direction. For example, the morphology and alignment of the cells show actin directionality of approximately 90° (Figure 7d(3)). In contrast, the control sample (Figure 7a) and the sample with pattern II (Figure 7c) produced curves devoid of distinct peaks and broader distributions revealing no defined actin alignment (Figure 7a(3) and 7c(3), respectively). Therefore, these microdomains can be used to control the cell morphology and organization. However, these scaffolds did not yield significant differences in the proliferation rate of hMSCs (Figure 7e). Differentiation of hMSCs into osteogenic and adipogenic lineages also showed insignificant differences (data not shown).

### 3.9. Effect of Micropatterned Scaffolds on Cell Migration

In addition to demonstrating that the PLLA scaffolds with different microtopography structures affected the morphology of hMSCs, the effect on cell migration was examined by using isolated DRG tissues (Figure 8). Image J analysis indicated that the ratio of the area covered by migrated cells to the initial DRG tissue area for the control sample (Figure 8a) and the samples with pattern I, II, and III (Figure 8b–d) is equal to 3.2, 7.5, 6.7, and 8.6, respectively. In the case of the flat (control) scaffold, Schwann cell migration was mainly confined within the immediate region surrounding the DRG tissue and did not show any particular directionality due to the random fiber orientation and high fiber density (Figure 8a). In contrast, Schwann cell migration from the DRG tissue was significantly enhanced on the organized fiber structure of the micropatterned scaffolds, with a much larger area around the DRG tissue covered by Schwann cells (Figure 8b–d). Fiber alignment, either in the diagonal (pattern I, Figure 8b) or parallel (pattern III, Figure 8d) direction, promoted cell migration along the fiber direction. Since the density and alignment of the fibers for pattern II (Figure 8c) are not significantly different from that of the control scaffold, it may be inferred that the 3D structure was conducive to Schwann cell migration out of the DRG tissue.

### 3.10. Effect of Micropatterned Scaffolds on Cell Infiltration

Characteristic cross-sections of different PLLA fibrous scaffolds (Figure 9) reveal *in vivo* cell infiltration and allow for quantitative comparison of the observed cell infiltration based on cell distribution (in cells/mm$^2$). In the case of the control sample possessing a dense structure with randomly oriented fibers, cell infiltration through the scaffold thickness was limited, with the cells mostly confined within the near-surface region (Figure 9a). However, the scaffold with pattern I (Figure 9b) shows increased cell infiltration from both sides in the less dense regions exhibiting fiber alignment (Figure 9b(A-A)), as opposed to limited cell infiltration in the small microwells possessing a dense fiber structure at the back side of the scaffold (Figure 9b(B-B)). Nevertheless, the scaffold with pattern I (Figure 9b) shows more profound cell infiltration compared to the control scaffold (Figure 9e).

For scaffolds with pattern II (Figure 9c), cell infiltration through the cross-section of microwells (Figure 9c(A-A)) is similar to the control sample, except the region near the border of the microwells, whereas cell infiltration through the cross-section of the regions between the microwells (Figure 9c(B-B)) is more pronounced. However, even though

overall infiltration is higher than that of the control scaffold (Figure 9e), these regions represent a very small fraction of the total scaffold surface area. Similar results were obtained for scaffolds with pattern III (Figure 9d). More enhanced cell infiltration in less dense regions of aligned fibers is shown in Figure 9d(A-A), similar to that for the scaffold with pattern I (Figure 9b(A-A)). Conversely, reduced cell infiltration in regions of randomly oriented dense fibers, especially at the back side of the scaffold is shown in Figure 9d(B-B), similar to that for the scaffold with pattern II (Figure 9c(A-A)). In general, more uniform and deeper cell infiltration occurred in scaffold regions of less dense and aligned fibers (Figure 9b(A-A), c(B-B), and d(A-A)), while regions of densely packed and randomly oriented fibers confined the cells to the surface (Figure 9a, b(B-B), c(A-A), and d(B-B)). Despite the higher fiber density at the front side of the micropatterned scaffolds compared to the region with aligned fibers at the back side of the scaffold (Figure 5), the cell infiltration results shown in Figure 9b–c indicate an enhancement and local selection of cell infiltration *in vivo* (Figure 9e).

## 4. CONCLUSIONS

Silicon wet etching and PDMS molding techniques were combined in this study to construct micropatterned templates, which were subsequently used to fabricate fibrous PLLA scaffolds by electrospinning. To control the fiber conformity, scaffolds with significantly different fibrous structures were fabricated by varying the geometry of micropattern features on the PDMS templates and the feed rate of the electrospun polymer solution. Because silicon wet etching and PDMS molding are versatile fabrication techniques, PDMS templates with a wide range of micropatterns were fabricated with the present method. The results of this study indicate that the developed method can easily be used to fabricate fibrous structures with different characteristics, including fiber alignment, locally high/low porosity (density), and microwells of different dimensions for a variety of biological applications. The fabricated micropatterned fibrous scaffolds were shown to significantly affect the cell morphology and enhance cell migration *in vitro* and cell infiltration *in vivo* for potential cell and tissue engineering applications.

## Supplementary Material

Refer to Web version on PubMed Central for supplementary material.

## Acknowledgments

The silicon master wafer was fabricated at the Berkeley Nanofabrication Laboratory. The authors thank Dr. Z. Yan for assistance in sample implantation and extraction in the *in vivo* experiments, Dr. H. Jeon and Prof. C. Grigoropoulos for sample sectioning by laser cutting, and Dr. A. Wang for assistance in *in vitro* DRG tissue isolation and culture. This research was supported in part by the National Institute of Health (HL083900 and EB012240).

## References

1. Huang Z-M, Zhang Y-Z, Kotaki M, Ramakrishna S. Comp Sci Technol. 2003; 63:2223–2253.
2. Li D, Xia Y. Adv Mater. 2004; 16:1151–1170.
3. Jang J-H, Castano O, Kim H-W. Adv Drug Deliv Rev. 2009; 61:1065–1083. [PubMed: 19646493]
4. Lutolf MP, Gilbert PM, Blau HM. Nature. 2009; 462:433–441. [PubMed: 19940913]
5. Wang Y, Wang G, Chen L, Li H, Yin T, Wang B, Lee JC-M, Yu Q. Biofabrication. 2009; 1:015001. [PubMed: 20811096]
6. Zhang X, Reagan MR, Kaplan DL. Adv Drug Deliv. 2009; 61:988–1006.
7. Zhou Y, Yang D, Chen X, Xu Q, Lu F, Nie J. Biomacromolecules. 2008; 9:349–354. [PubMed: 18067266]

8. Chew SY, Wen J, Yim EKF, Leong KW. Biomacromolecules. 2005; 6:2017–2024. [PubMed: 16004440]
9. Thorvaldsson A, Stenhamre H, Gatenholm P, Walkenström P. Biomacromolecules. 2008; 9:1044–1049. [PubMed: 18260633]
10. Mei F, Zhong J, Yang X, Ouyang X, Zhang S, Hu X, Ma Q, Lu J, Ryu S, Deng X. Biomacromolecules. 2007; 8:3729–3735. [PubMed: 18020395]
11. Huang NF, Patel S, Thakar RG, Wu J, Hsiao BS, Chu B, Lee RJ, Li S. Nano Lett. 2006; 6:537–542. [PubMed: 16522058]
12. Patel S, Kurpinski K, Quigley R, Gao H, Hsiao BS, Poo M-M, Li S. Nano Lett. 2007; 7:2122–2128. [PubMed: 17567179]
13. Kurpinski KT, Stephenson JT, Janairo RRR, Lee H, Li S. Biomaterials. 2010; 31:3536–3542. [PubMed: 20122725]
14. Zhu Y, Wang A, Patel S, Kurpinski K, Diao E, Bao X, Kwong G, Young WL, Li S. Tissue Eng Part C: Methods. 2011; 17:705–715. [PubMed: 21501089]
15. Chew SY, Mi R, Hoke A, Leong KW. Biomaterials. 2008; 29:653–661. [PubMed: 17983651]
16. Hwang Y-S, Chung BG, Ortmann D, Hattori N, Moeller H-C, Khademhosseini A. Proc Nat Acad Sci USA. 2009; 106:16978–16983. [PubMed: 19805103]
17. Nam J, Huang Y, Agarwal S, Lannutti J. Tissue Eng. 2007; 13:2249–2257. [PubMed: 17536926]
18. Pham QP, Sharma U, Mikos AG. Biomacromolecules. 2006; 7:2796–2805. [PubMed: 17025355]
19. Soliman S, Sant S, Nichol JW, Khabiry M, Traversa E, Khademhosseini A. J Biomed Mater Res A. 2011; 96:566–574. [PubMed: 21254388]
20. Baker BM, Gee AO, Metter RB, Nathan AS, Marklein RL, Burdick JA, Mauck RL. Biomaterials. 2008; 29:2348–2358. [PubMed: 18313138]
21. Lee BL-P, Jeon H, Wang A, Yan Z, Yu J, Grigoropoulos C, Li S. Acta Biomater. 2012; 8:2648–2658. [PubMed: 22522128]
22. Teo WE, Ramakrishna S. Nanotechnol. 2006; 17:R89–R106.
23. Blakeney BA, Tambralli A, Anderson JM, Andukuri A, Lim D-J, Dean DR, Jun H-W. Biomaterials. 2011; 32:1583–1590. [PubMed: 21112625]
24. Vaquette C, Cooper-White JJ. Acta Biomater. 2011; 7:2544–2557. [PubMed: 21371575]
25. Li D, Ouyang G, McCann JT, Xia Y. Nano Lett. 2005; 5:913–916. [PubMed: 15884893]
26. Zhang D, Chang J. Adv Mater. 2007; 19:3664–3667.
27. Zhang D, Chang J. Nano Lett. 2008; 8:3283–3287. [PubMed: 18767890]
28. Li J, Yi X. Appl Phys A: Mater Sci Proc. 2010; 98:757–760.
29. Ding Z, Salim A, Ziaie B. Langmuir. 2009; 25:9648–9652. [PubMed: 19705879]
30. Fridrikh SV, Yu JH, Brenner MP, Rutledge GC. Phys Rev Lett. 2003; 90:144502. [PubMed: 12731920]

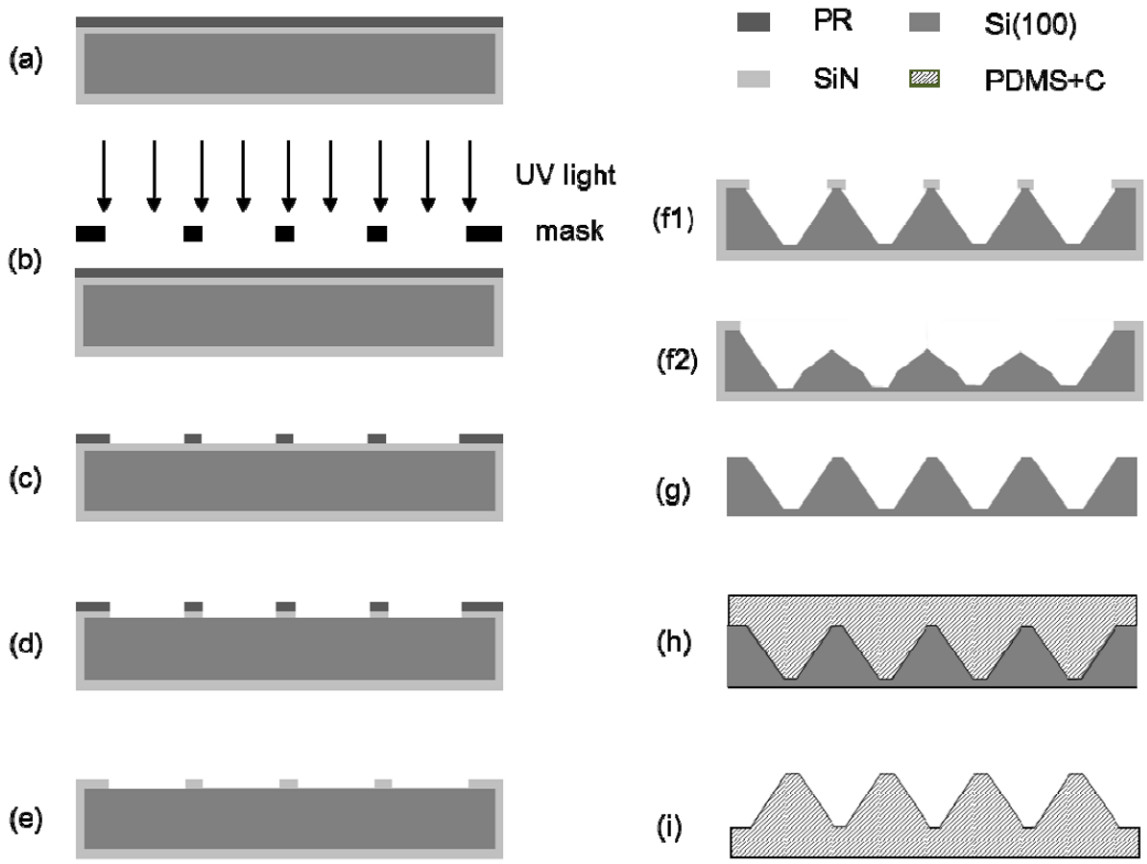


**Figure 1.**

Schematic of the PDMS template fabrication process: (a) spin coating of the back side of a SiN-coated Si(100) wafer with PR, (b) PR exposure to UV light, (c) PR development, (d) removal of the exposed SiN layer by RIE, (e) PR stripping, (f1,f2) wet etching with 30% KOH, (g) removal of the SiN layer in (f1) by wet etching with 49% HF, (h) molding of the conductive (12.5% w/v carbon black in silicon mixture) PDMS template using the master wafer shown in (g), and (i) lift-off of the PDMS template produced from the master wafer shown in (g).

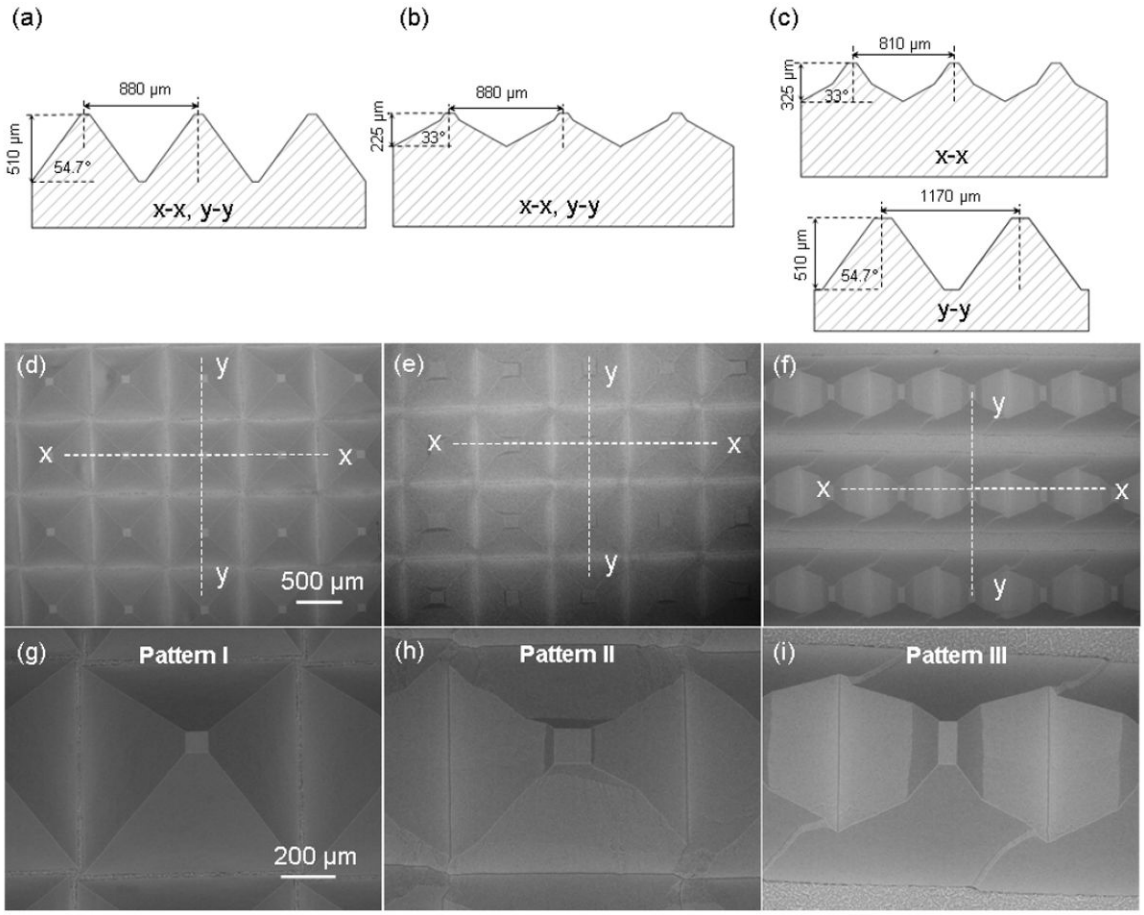


**Figure 2.**
Schematics and dimensions of PDMS templates with (a) pattern I, (b) pattern II, and (c) pattern III. (d)–(i) SEM micrographs of templates with pattern I, II, and III, respectively.

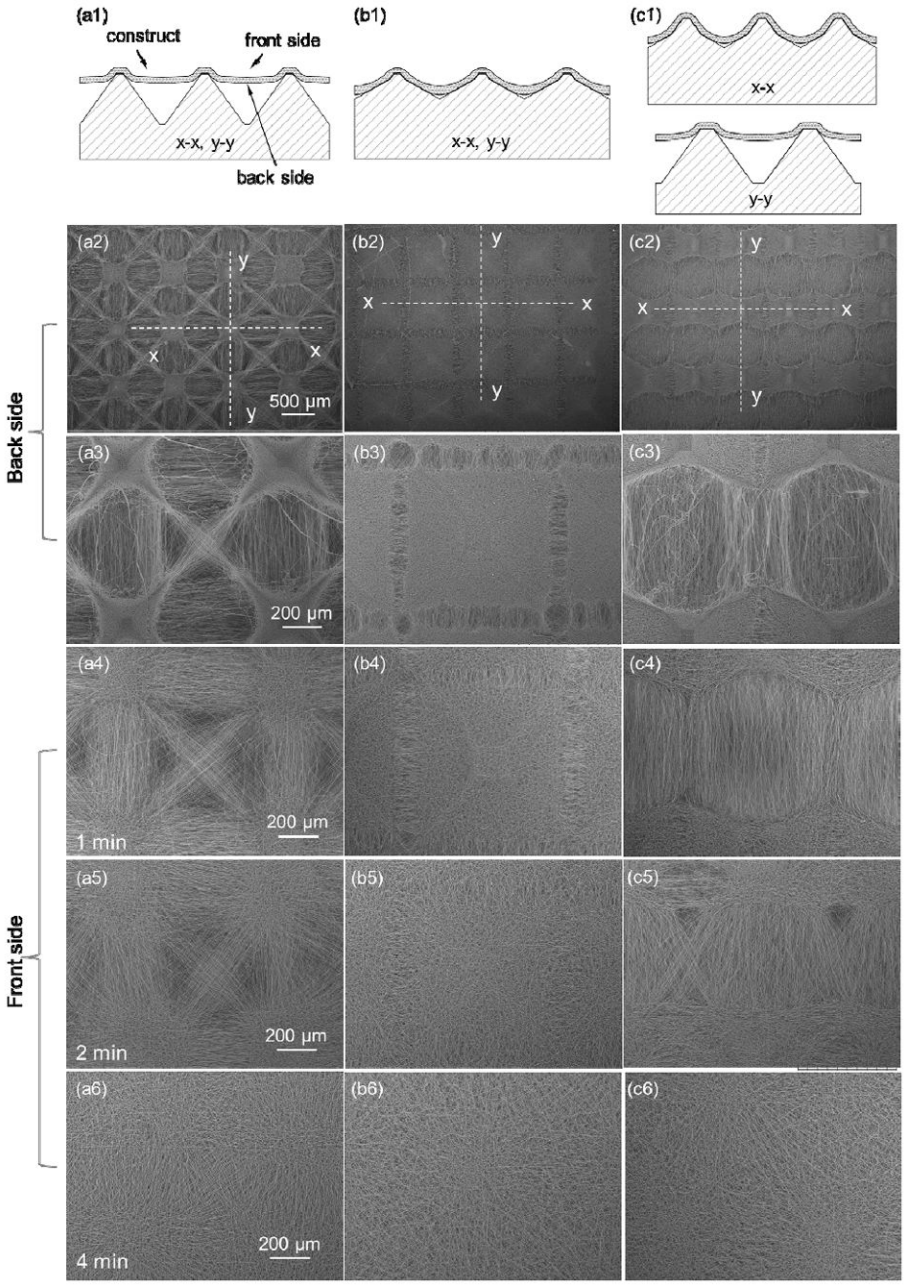


**Figure 3.**

Effects of template micropattern and deposition time on fiber surface coverage and alignment: (a1), (b1), and (c1) schematics of PLLA fiber deposition on PDMS templates with pattern I, II, III, respectively, and SEM micrographs of (a2)–(c3) back side and (a4)–(c6) front side of PLLA fibrous scaffolds.

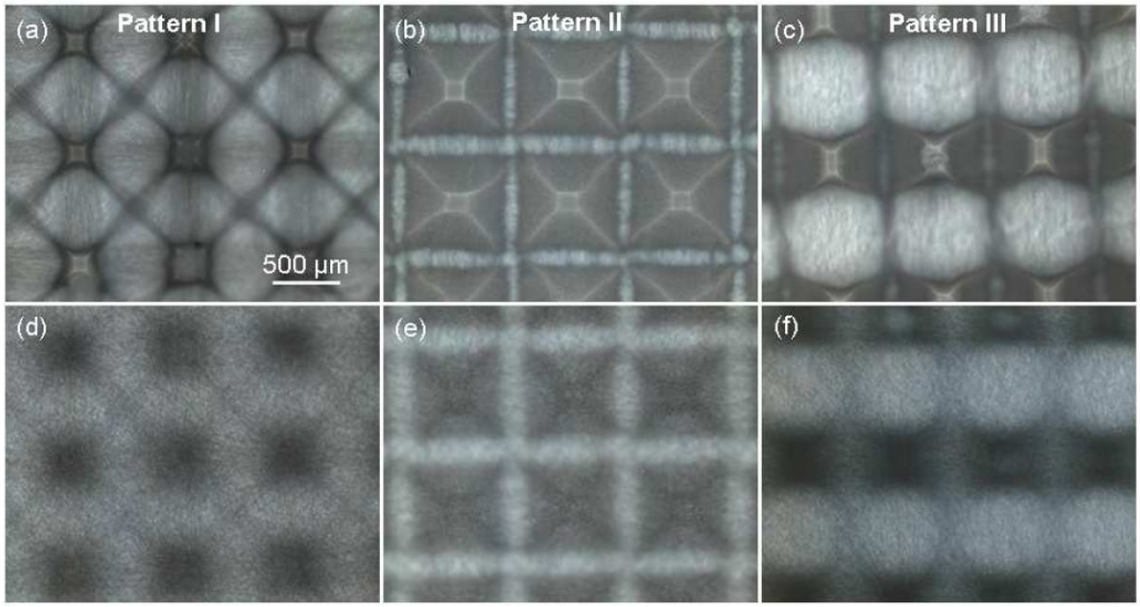


**Figure 4.**
Optical photographs of PLLA fibrous scaffolds fabricated with PDMS templates with pattern I, II, and III: (a)–(c) back side and (d)–(f) front side of the micropatterned scaffolds.

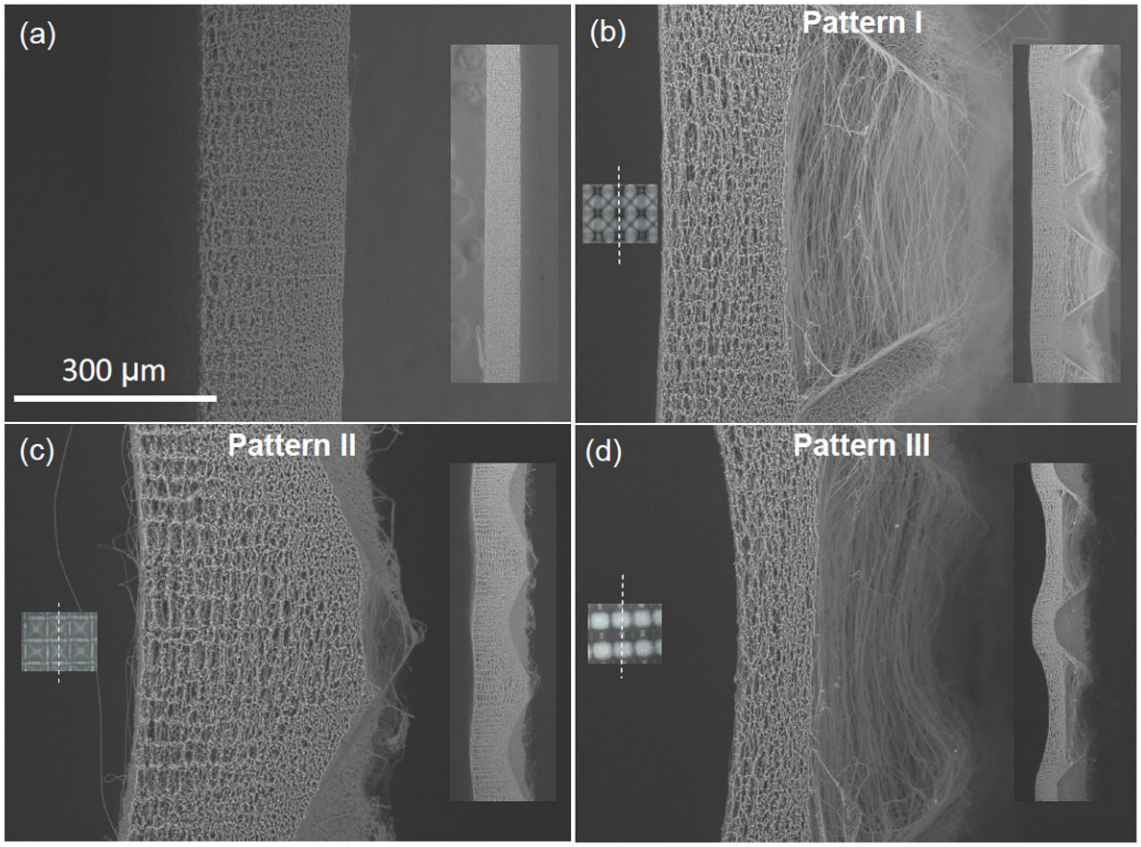


**Figure 5.**
Cross-sectional SEM images of PLLA fibrous scaffolds fabricated with (a) flat (control) and (b)–(d) PDMS templates with pattern I, II, III, respectively. Insets on the left show corresponding optical images of the scaffolds and the laser cutting line (dot line), whereas insets on the right show lower magnification cross-sectional images of the scaffolds. The right side of the scaffolds was in contact with the PDMS template.

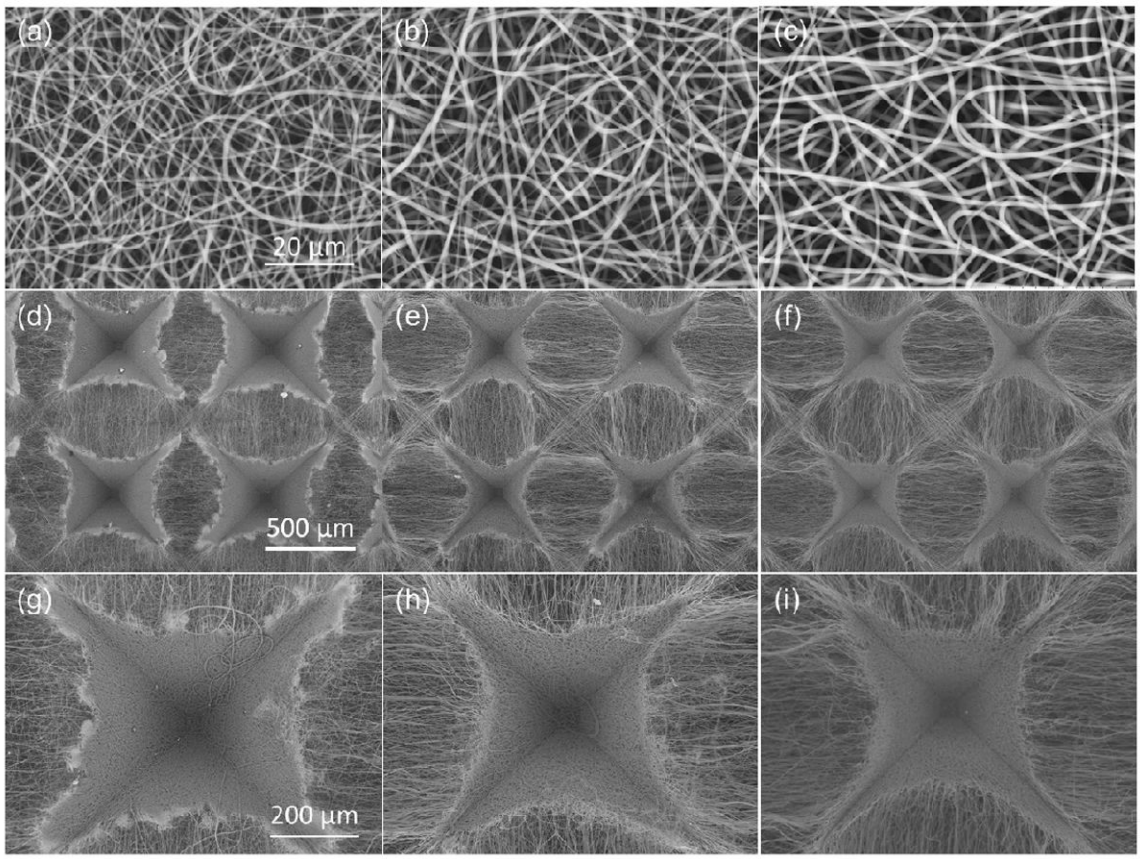


**Figure 6.**
Feed rate effect of PLLA solution on the micropattern of electrospun PLLA scaffolds: (a)–(c) PLLA fibers deposited on a flat PDMS template, (d)–(f) SEM images of PLLA fibrous scaffolds fabricated on templates with single-slope pyramidal posts (pattern I), and (g)–(i) high-magnification SEM images of the scaffolds shown in (d)–(f) illustrating the formation of individual microwells. Fiber electrospinning was carried out at a feed rate of (a), (d), and (g) 0.2 mL/h, (b), (e), and (h) 0.5 mL/h, and (c), (f), and (i) 2 mL/h.

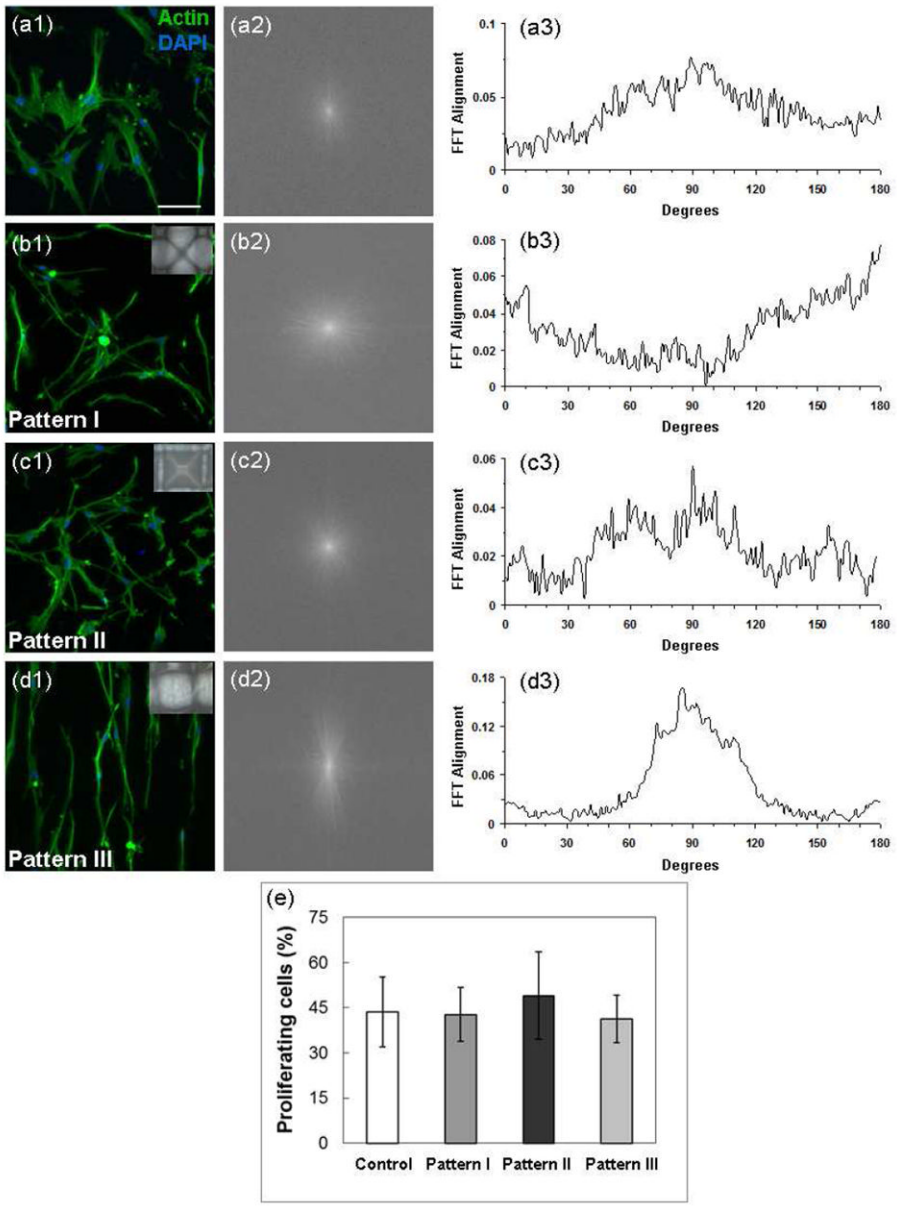


**Figure 7.**

Effect of micropatterned scaffolds on cell morphology, organization, and proliferation. Morphology and organization of hMSCs seeded and cultured on (a1) flat (control) and micropatterned PLLA fibrous scaffolds with (b1) pattern I, (c1) pattern II, and (d1) pattern III visualized by actin staining. Actin alignment quantified by (a2–d2) Image J frequency plots and (a3–d3) 2D FFT alignment plots. (e) Proliferation rate of hMSCs after *in vitro* culture on PLLA fibrous scaffolds for 24 h (n = 3): (a) flat (control) scaffold with dense and randomly oriented fibers and (b)–(d) scaffolds with pattern I, II, and III, respectively. The inset in (b)–(d) shows an image of the corresponding micropatterned scaffold.

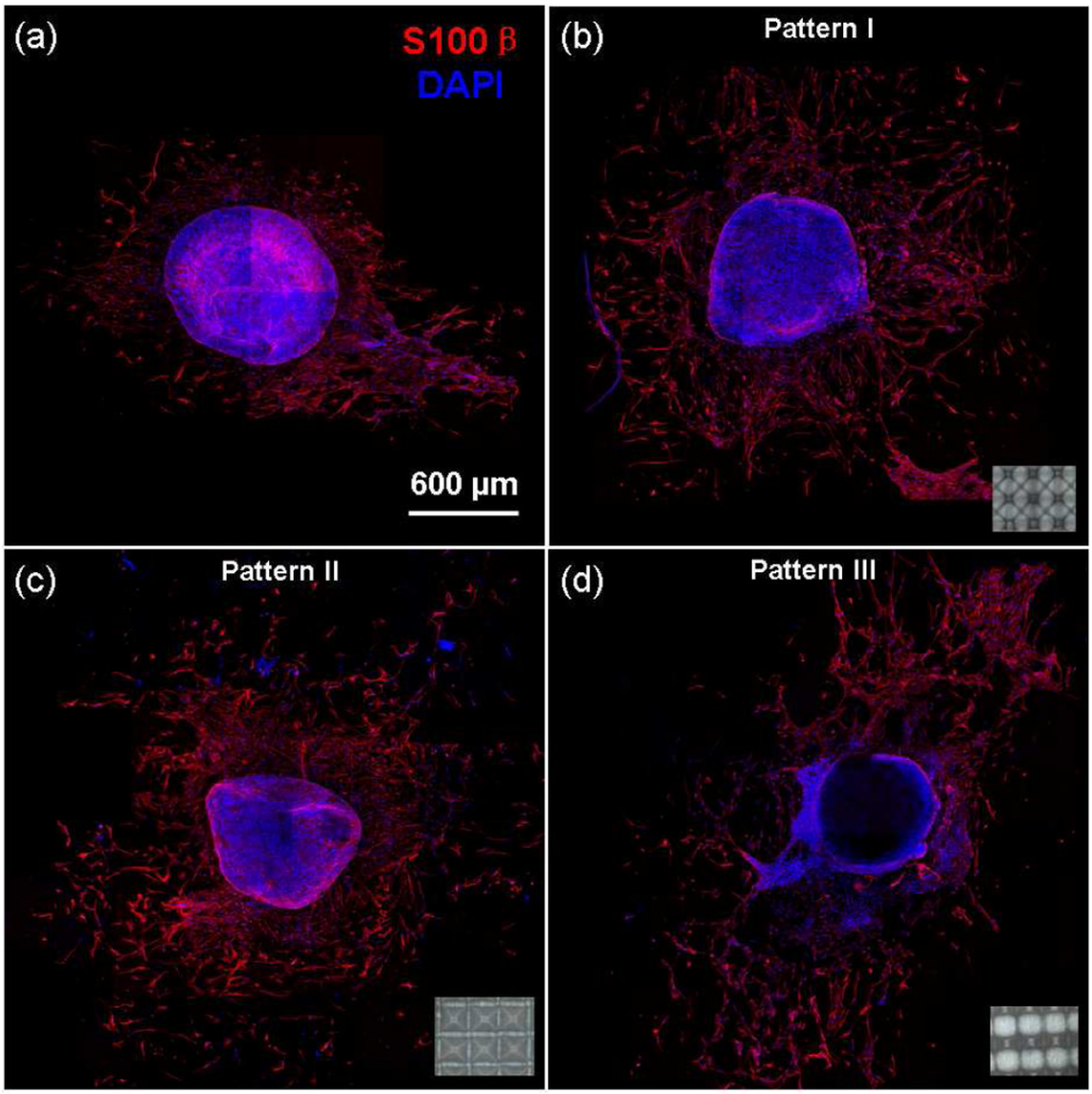


**Figure 8.**

*In vitro* migration of Schwann cells on (a) a flat (control) and micropatterned PLLA fibrous scaffolds with (b) pattern I, (c) pattern II, and (d) pattern III. Insets show corresponding optical images of the micropatterned scaffolds.

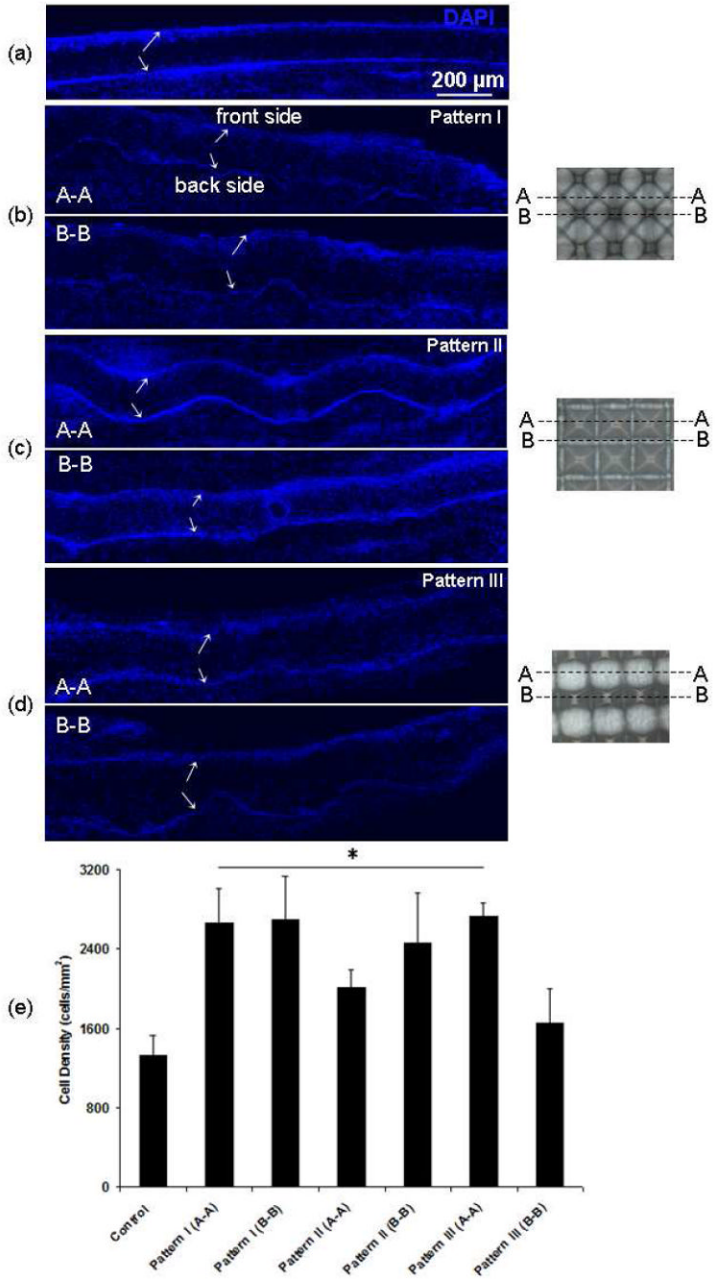


**Figure 9.**

Cross-sections of PLLA fibrous scaffolds showing cell infiltration after *in vivo* implantation in the subcutaneous cavity of rats for 7 days: (a) flat (control) PLLA scaffold with dense and randomly oriented fibers and micropatterned PLLA fibrous scaffolds with (b) pattern I, (c) pattern II, and (d) pattern III. Arrows indicate the top (front side) and bottom (back side) boundaries of the scaffolds. Boxes in cross-section A-A shown in (c) indicate regions near the border of the microwells. Images on the right show cross-sections A-A and B-B corresponding to the fluorescence images of each micropatterned scaffold shown in (b)–(d). (e) Quantification of cell infiltration based on cell distribution (cells/mm$^2$) through the scaffold thickness (n = 4). Statistically significant differences ($p < 0.05$) compared to the control scaffold are indicated by an asterisk (*).

**Table 1**

Summary of commonly used patterned templates for electrospinning.

| Fabrication process | Scaffold organization | Controllability | Reference |
|---|---|---|---|
| Metal plate with holes or nonconductive region | Plane scaffold with porous regions or regions with aligned fibers | No precise control of the pattern size and scaffold structure | 24, 25 |
| Metal wire | Porous fibrous structure with aligned fibers | No precise control of the pattern size and scaffold structure | 5, 24 |
| Metal posts on a plane surface or a 3D structure | 2D/3D porous structure with fiber alignment | Pattern size depends on metal machining resolution | 26, 27 |
| Spherical dish with a metal array | Porous fibrous structure | Control only of the porosity of the fibrous structure | 23 |

**Table 2**

Effect of feed rate on the diameter of electrospun fibers ($n \geq 42$).

| feed rate (mL/h) | fiber diameter (nm) |
|---|---|
| 0.2 | 599.0 ± 177.1 |
| 0.5 | 790.2 ± 317.9 |
| 2.0 | 933.0 ± 288.7 |